# Ion Transport in the Return Flow Ion-Concentration-Polarization System

*Dung T. Nguyen, Khai H. Nguyen, Van-Sang Pham**

*School of Transportation Engineering, Hanoi University of Science and Technology, Ha Noi, Vietnam*
*\*Corresponding author email: sang.phamvan@hust.edu.vn*

**Abstract**

*The novel desalination device, the return flow electromembrane desalination called Return Flow Ion-Concentration-Polarization (RF-ICP) which resolved one of the most prominent problems in ICP is the over-limiting conduction mechanism. The development of the ion depletion layer largely determines the energy consumption of electromembrane desalination, because of the increased electrical resistance of the ion-depleted boundary layer which is also a desired outcome for desalination. In this work, we conducted a study on the desalination efficiency of the RF-ICP desalination system for different operations. The transport of ions in the system was examined by using numerical simulation. The Poisson-Nernst-Planck and Navier-Stokes equations were solved numerically to model the transport of ions at different electrical current regimes and the feeding-flow rates. Obtained simulation results showed that the current and current efficiency increases with the feeding-flow rate, the salt removal ratio changes inversely with feeding-flow rate, and the energy per ion remove decreases when increasing the feeding-flow rate. The findings are useful in optimizing the design and operation of the RF-ICP desalination system.*

Keywords: Electrical desalination, ions transport, numerical simulation, Poisson-Nernst-Planck-Navier-Stokes equations.

## 1. Introduction

Desalination is a process that extracts salts and minerals from saline water [1]. In the field of desalination, there are various desalination technologies, that include solar distillation, natural evaporation, vacuum distillation, multi-stage flash distillation, multiple-effect distillation, vapor-compression distillation, reverse osmosis, electrodialysis membrane, membrane distillation. Among them, reverse osmosis (RO) which has reached an energy consumption ($\sim$3 kWh/m$^3$) that is approaching the theoretical minimum ($\sim$1 kWh/m$^3$, for 35 g/kg feed with 50% recovery is considered the leading technology [2, 3]. The operation efficiency of RO has been significantly improved over the last two decades, mainly by energy recovery and other optimizations [4]. The volume of brine generation is consistently increasing because of the ever-increasing desalination capacity brought on by economic growth. Additionally, more concentrated brine (50-85 g/kg) [5] has been produced as a result of effective desalination operations and better recoveries of pure product water, making treatment more difficult. The production of large amounts of hypersaline brine effluent (8-360 g/kg) [6-9] as a result of current oil/gas extraction methods is another factor that is being recognized as a hazard to the environment. The gas sector frequently hauls away brine waste and deposits it in permitted injection wells without additional treatment due to a lack of cost-effective treatment methods, which might seriously contaminate ground water resources in adjacent areas [10, 11]. Unfortunately, the RO membrane modules are not typically constructed for the hydraulic pressure required to overcome the large osmotic pressure, which results from the substantial salinity difference between the feed and the permeate, for high salinity feed with salinity exceeding seawater level (35 g/kg) [12]. On the other hand, electromembrane desalination can be more advantageous in treating high salinity brine due to the flexibility of control of the salt removal ratio of output product without any upper limit of feed salinity [13, 14]. The electromembrane desalination technologies were moreover reported that they are less energy input at any salinity than the thermal desalination systems such as mechanical vapor compression (MVC) humidification-dehumidification (HDH) which are also the alternative solution for the problem of treating the high salinity brine [15]. Once brine waste salinity is brought down to levels comparable to those of seawater, a variety of other technical alternatives are available to treat the wastewater even more effectively than such a nearly complete treatment [16].

In our previous work, we introduced a novel desalination device, the return flow (RF) electromembrane desalination called return flow ion concentration polarization (RF-ICP) which controls the flow path that effectively limits the growth of the ion depletion region and results in both high salt

removal and high energy efficiency. Our modeling and experiment observations indicated that the system could improve desalination efficiency with a higher salt removal ratio at similar power consumption compared to the batch electrodialysis (ED) system while using much less membrane area [17]. ICP desalination is based on the examination of the ion transport characteristics across the ion exchange membrane, specifically in this case the diffusivity coefficient of sodium ion and chloride ion [18]. This is because sodium chloride salt predominates in the feeding sources. Instead of desalination employing cation exchange membrane (CEM) and anion exchange membrane (AEM) as in ED desalination, ICP uses unipolar ion conduction by employing CEM which is considered as a cation filter by allowing only cation to pass through to enhance an energy efficiency using the higher diffusivity of chloride ion. The novel architecture RF-ICP is the potential of being a solution for the most prominent problem in ICP is the over-limiting conduction (OLC) mechanism.

In this work, using numerical modeling, we will examine theoretically the performance of the RF-ICP by studying ion transport in the system. The simulations were carried out using an in-house code that solved a coupling of the Poisson-Nernst-Planck (PNP) equations and Navier-Stokes (NS) equations [19-21]. The same membranes-inter-distances are considered at various flow rates and applied voltage to elucidate their impact on the desalination efficiency of the system.

## 2. Return Flow Desalination Device

Fig. 1a provides a schematic representation of the return flow electromembrane desalination system that uses the ion RF-ICP. The three channels are separated by two porous membranes, and the ends of the channels are linked to divide the input stream in the central channel into streams in the side channels. Between two membranes, a bias voltage is provided, creating a consistent electric field that points from the upper CEM to the lower CEM. The specifics of the RF-ICP design are described in our previous paper [17].

To examine the energy efficiency and desalination capacity of the return flow ion concentration polarization system, we simulated the system using an in-house code. During the process, we use two CEMs on the outermost side, the distance between them is 3.2 mm, in the middle, there are two porous membranes placed parallel to CEMs and symmetrical with each other. Two porous membranes split the system into three distinct channels with a thickness of the dilute channel (0.8 mm), intermediate channel (1.6 mm), and concentrate channel (0.8 mm). This clear separation results from the return flow induced by the one-sided closure of the system. The total length of the system is 8 mm, in which the

distance from the end of the porous membrane to the wall boundary is 3.2 mm.

## 3. Numerical Model and Method

### 3.1. Governing Equations and Boundary Conditions

#### 3.1.1. Governing Equations.

To conduct numerical simulation for the transport of ions in the RF system, we use the model sketched in Fig. 1b. Appropriate boundary conditions are involved in modeling the electrical and mechanical behavior of ion species, potential, and fluid flow. In the progress of applying the numerical method to solving the problem, we discretized the computation domain through the meshing stage as shown in Fig. 2. The mathematical form of the boundary condition will be described in the latter part of this section.
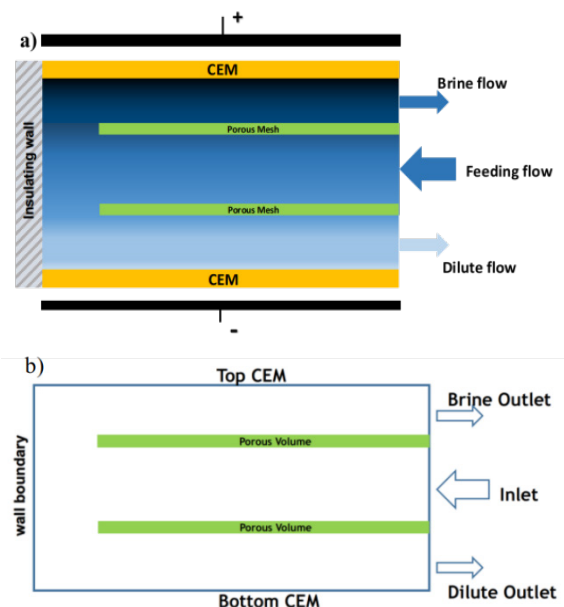


Fig. 1. Schematic illustration of ion concentration polarization system (a) and the corresponding computation domain model (b).
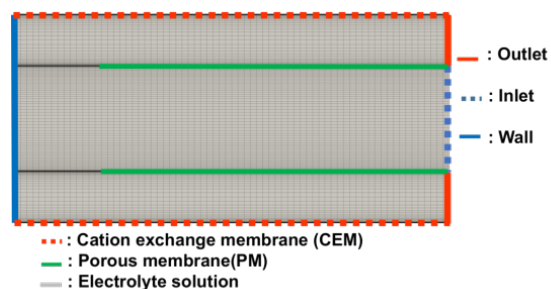


Fig. 2. The mesh used in simulation and refined cells near the charged surface to resolve the nonlinearity of the variables.

Ions move within the system under the influence of the electric field, diffusion, and convection of fluid flow. The ions transportation is governed by the

Nernst-Planck equations (1) and (2); the mutual effect of electric potential field and ion concentrations is demonstrated by Poisson equation (3) and (4), and the motion of the fluid is described by the Navier-Stokes equations (3.1.5) and (3.1.6). The dimensionless form of these equations is as follows:

$$\frac{1}{\tilde{\lambda}_D} \partial \frac{\tilde{C}_\pm}{\partial \tilde{t}} = -\tilde{\nabla} \cdot \tilde{\mathbf{J}}_\pm \tag{1}$$

$$\tilde{\mathbf{J}}_\pm = -\tilde{D}(\tilde{\nabla}\tilde{C}_\pm + Z_\pm \tilde{\nabla}\tilde{\Phi}) + P_e \tilde{\mathbf{U}}\tilde{C}_\pm \tag{2}$$

$$\tilde{\lambda}_D{}^2 \tilde{\nabla} \cdot (\tilde{\nabla}\tilde{\Phi}) = -\tilde{\rho}_e \tag{3}$$

$$\tilde{\rho}_e = Z_+ \tilde{C}_+ + Z_- \tilde{C}_- \tag{4}$$

$$\frac{1}{Sc}\frac{1}{\tilde{\lambda}_D}\frac{\partial \tilde{\mathbf{U}}}{\partial \tilde{t}} = -\tilde{\nabla}\tilde{P} + \tilde{\nabla}^2\tilde{\mathbf{U}} - Re(\tilde{\mathbf{U}} \cdot \tilde{\nabla})\tilde{\mathbf{U}} -$$
$$\frac{1}{\tilde{\lambda}_D{}^2}\tilde{\rho}_e \tilde{\nabla}\tilde{\Phi} \tag{5}$$

$$\tilde{\nabla} \cdot \tilde{\mathbf{U}} = 0 \tag{6}$$

where $\tilde{t}$, $\tilde{C}_\pm$, $\tilde{\Phi}$, $\tilde{\mathbf{U}}$ and $\tilde{P}$ denote the dimensionless time, concentration of cations (+) and anions (-), electric potential, vector of fluid velocity, and pressure, respectively. These quantities are normalized by the corresponding reference values of time, ionic concentration, electric potential, velocity, and pressure, respectively as follows:

$$\tau_0 = \frac{l_0{}^2}{D_0}; \Phi_0 = \frac{k_B T}{Z_e}; C_0 = C_{\text{bulk}};$$

$$U_0 = \frac{\varepsilon \Phi_0}{\eta l_0}; P_0 = \frac{\eta U_0}{l_0} \tag{7}$$

where $C_0$ is the concentration scale, $l_0$ is the characteristic length scale, $D_0$ is the average diffusion, $k_B$ is the Boltzmann constant, $T$ is the absolute temperature, $e$ is the elementary charge, $Z = |Z_\pm|$ is ion valence, $\eta$ is the dynamic viscosity of the solution, and $\varepsilon$ is the permittivity of the solvent. Parameters $\tilde{D}_\pm = \frac{D_\pm}{D_0}$, $\tilde{\lambda}_D = \frac{\lambda_D}{l_0}$, and $\tilde{\rho}_e = \frac{\rho_e}{C_0}$ are dimensionless diffusion coefficient, the Debye length, and the space charge, respectively. $Pe = U_0 \frac{l_0}{D_0}$, $Sc = \frac{\eta}{\rho_m} D_0$, and $Re = U_0 l_0 \frac{\rho_m}{\eta}$ are the Péclet number, the Schmidt number, and the Reynolds number, respectively. Value of the potential scale ($V_0$) and ion current scale ($I_0$) 25.85 mV, 1.62 mA, respectively.

*3.1.2. Boundary conditions:*

At the Inlet, the boundary condition for fluid flow is constant laminar inflow given at the feeding velocity value; the concentration of both cations and anions are also given and remains constant during system operation that represents the actual configuration in which the inlet connects to an electrolyte solution tank; the electric potential is assumed to be floating:

$$C_+ = C_- = C_0; \mathbf{U} = U_{feeding}$$

$$\frac{\partial \Phi}{\partial n} = 0$$

At the outlet, the free-stream condition is applied for the transportation of both fluid and ions concentration. The electric potential is also assumed to be floating.

$$\frac{\partial C_+}{\partial n} = \frac{\partial C_-}{\partial n} = \frac{\partial U}{\partial n} = \frac{\partial \Phi}{\partial n} = 0$$

On the CEM boundaries, to mimic the permselective feature of the membrane, a fixed value condition is applied for cation concentration, while no ionic flux condition is enforced for anions; the no-slip condition is applied for fluid flow; the electric potential is given at the membranes to enforce a downward electric field that defines the ions transport in the system:

$$C_+ = 2C_0; J_- = 0; \mathbf{U} = 0$$

$$\Phi = 0: \text{On the bottom CEM}$$

$$\Phi = \Phi_{applied}: \text{On the bottom CEM}$$

In this model, the porous membranes (PM) are considered to be thin enough, so that electromigration and diffusion of ions across these membranes are no different from that in the electrolyte solution. In other words, the PNP equations remain the same form in the solution and porous membranes. This assumption reflects most of the physics occurring in PMs which are PCTE0220030, Sterlitech Co., Kent, WA, USA, and whose thickness accounts for 0.15% of the system's thickness [17]. Due to high fluidic viscous resistance, as fluid derives across the PM and the thinness of the membrane, it is possible to make an assumption of a given fluid velocity leaking through the PM. In this work, we assume that 10% of feeding-flow leaks through the PM, correspondingly, the value of $0.1U_{feeding}$ is taken for the velocity of the fluid through the PM.

To investigate the efficiency of the RF-ICP system, some important parameters are considered. The first parameter is current efficiency (CE), which describes how effective ions can be separated by ion-exchange membrane for an applied current, and is given by:

$$CE = \frac{zFQ_{dilute}(C_0 - C_{dilute})}{2NI} \tag{8}$$

where $C_0$ and $C_{dilute}$ are concentrations of initial and dilute flow, respectively, $z$ is ion's charge, $F$ is the Faraday constant (96,485 C/mol), $Q_{dilute}$ is flow rate, $N$ is the number of cell pairs and I is the current.

Second, to determine the desalination ability of RF-ICP system, we calculate the salt removal ratio (SRR) from the initial concentration of flow $C_0$ and that of the dilute flow $C_{dilute}$ as follows:

$$SRR = \frac{C_0 - C_{dilute}}{C_0} \tag{9}$$

To understand how efficiently the supplied energy for the RF-ICP system is used for rejections, energy per ion removal (EPIR), which is the energy needed to remove a single ion, is measured by dividing the total energy consumption by the number of removed ions:

$$\text{EPIR} = \frac{\frac{IV}{Q_{dilute}}}{k_{\text{B}}T(C_0 - C_{\text{dilute}})} \qquad (10)$$

### 3.2. Numerical Methods

Simulations were performed using an in-house code, which solved the above set of coupled Poisson-Nernst-Planck-Navier-Stokes equations directly on a two-dimensional domain. The PNP and NS equations are connected in a nonlinear manner. The convection term in the PNP equations and the electric body force in the NS equations serve as the links between these two sets of equations. We created a coupled approach for solving the sets of PNP and NS equations in order to avoid solving the complicated system of linear equations and ensure the strong coupling of the PNP equations and NS equations. The potential and ion concentrations are simultaneously solved from the PNP equations starting from a velocity field from the previous iteration or initial condition. The NS equations are then modified to include the electric body force. The PNP equations are then updated using the velocity field that was discovered by the solution of the NS equations. Up to convergence, the procedure is repeated as shown in Fig. 3. The equations are discretized using the locally conservative finite volume approach. The Newton-Raphson method is used to solve the nonlinear discretized PNP. The GMSH [22] is used to improve the mesh close to the membranes because of the rapid changes in the ion concentrations and electric potential in the electrical double layer (EDL).

## 4. Results and Discussion

To examine the response of the return flow system to the operation factors such as applied voltage and feeding-flow rate. We set up simulations with applied voltage increase from 0 $V_0$ to 40 $V_0$ for inlet feeding-flow velocity of 0.5 mm/s, 1.0 mm/s, and 1.5 mm/s corresponding to cases 1, 2, and 3, respectively. These values of velocities of the feeding flow are chosen according to the experimental results of our previous works [17]. If this value is too small, the advantages of the RF-ICP model that is limiting the development of the depletion region at the outlet of the system are not almost gained. When this value is too large, the viscous force exceeds the electric body force in the system, so the desalination capacity of the system is restricted. Since the thickness of the depleted region is almost unchanged when the flow reaches the outlet, the value of this feeding-flow velocity can be scaled when the length of the system change.

A mesh of 21140 cells was used to represent the computation domain (Fig. 2). The smallest mesh size is $4.73 \times 10^{-7}$, for the cells next to the membranes' surfaces. The largest mesh size is $2.0 \times 10^{-7}$, found in the cells at the channel center. All simulations were conducted using the M4800 Dell workstation with Intel i7, 2.4 Gh, processor, and 8 Gb of RAM. The running time for a single case is 32 seconds, approximately. Time-consuming happens mostly at the Poisson-Nernst-Planck equations solver. Validations for the numerical solver can be found in our previous works [18-20].
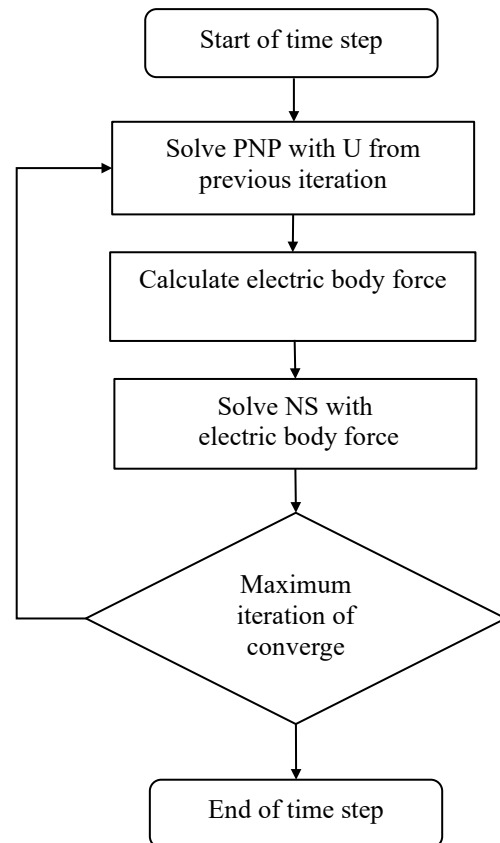


Fig. 3. The flow chart of simulation algorithm

### 4.1. Current-Voltage Response

The current-voltage response for the 3 cases is shown in Fig. 4, as can be seen, the ohmic and limiting current regimes are clearly shown. The ion distribution and fluid flow at the regimes are shown in Fig. 5.

Ohmic regime-found at the low applied voltages, in this regime, the current increases linearly with applied voltage for all cases. As the bias voltage between the anode and cathode increases, so does the current through the membrane with an increased slope coefficient corresponding to an increase in the velocities of feeding-flow. In other words, the same voltage is applied, the greater the velocity of the inlet flow, the greater the current through the membrane, and the higher its rate of rising.
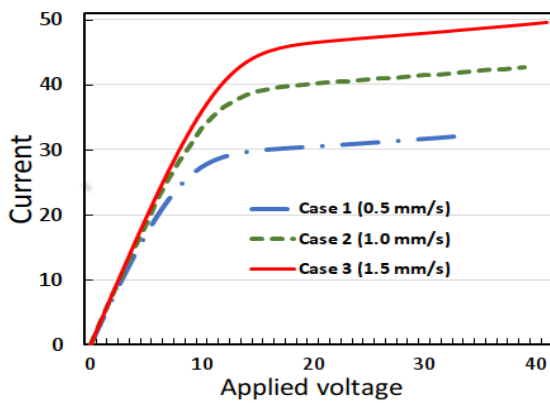
Fig. 4. The current-voltage curve measured at the various feeding-flow velocities: 0.5mm/s (dash-dot line); 1.0mm/s (dash line); 1.5mm/s (solid line).
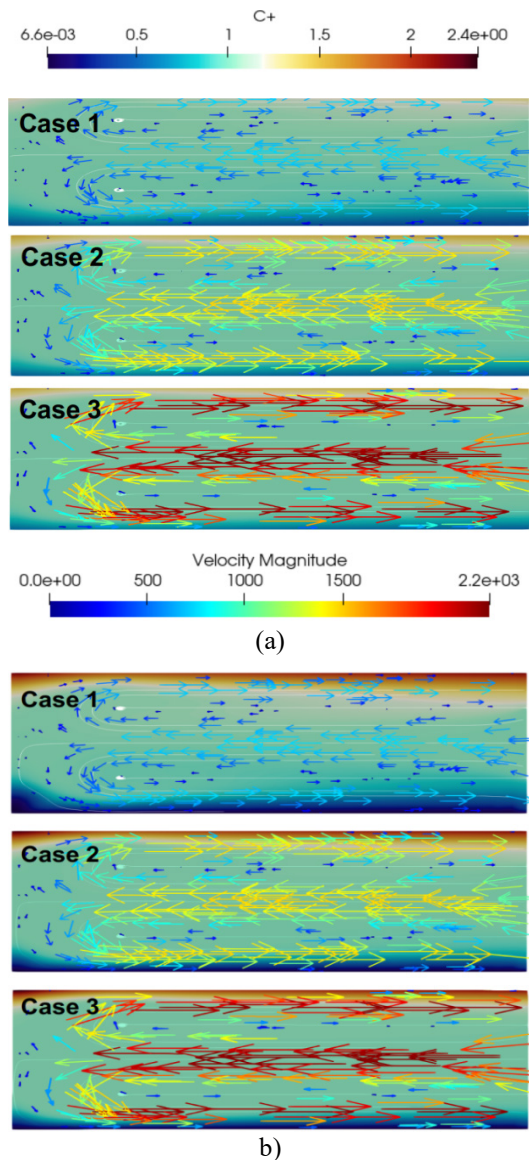


(a)



b)

Fig. 5. The ion distribution and fluid flow for the 3 cases: (a) the Ohmic regime, $5V_0$ and (b) the limiting current regime, $30V_0$.

Whereas, in the case of the velocity of the feeding-flow is 0.5 mm/s the system enters the limiting regime at the value of applied voltage ($\sim 13\ V_0$), these values are ($\sim 14\ V_0$) and ($\sim 16\ V_0$) corresponding to the velocities of inlet flows (1.0 mm/s) and (1.5 mm/s). This difference is explained by the characteristic of the rate of feeding-flow, the greater feeding-flow, the greater number of ions are carried into the channel that reduces the system resistance and so promotes the current passing through.

Limiting current regime-found at high applied voltage, at which the ions concentration at the solution layer next to membrane surface vanishes. In this regime, increasing applied voltage causes no corresponding current increase. That is due to the lack of current-carrying elements. Although the I-V curves of the three cases have similar slope coefficients, the value of current at the largest feeding-flow (i.e., 1.5 mm/s) is higher than the others, it is again due to the larger number of ions presenting in the channel. Considering the increase of limiting current with feeding-flow, as can be seen in Fig. 4, when the feed flow increases 0.5 mm/s from 0.5 mm/s to 1.0 mm/s, the current increases about $10\ I_0$. However, another 0.5 mm/s increase, from 1.0mm/s to 1.5 mm/s returns only $7\ I_0$ increase in current. It so indicates that there is a limit to increasing current by growing feeding-flow.

Fluid velocity vector field and ion concentration distribution in Ohmic ($5\ V_0$) a and limitting regimes ($30\ V_0$) are shown in Fig. 5. As can be seen, while the velocity vector field and streamlines seem to be identical among the regimes, the ion concentrations are different, especially, at the region next to the bottom CEM. That indicates the high polarization of ions near permselective membrane, as reposted in our previous works [18, 19, 20].

### 4.2. Effect of Feeding-Flowrate on the Vertical Distribution of Ions

To analyze the effect of feeding-flow velocity condition on the ion distribution in the system, we compared the distribution of the cation concentration at the dilute channel output of 3 cases 1, 2, 3 with feeding-flow velocities of 0.5 mm/s, 1.0 mm/s, and 1.5 mm/s, respectively. The results of concentration along a vertical line at the channel outlet for the three cases are shown in Fig. 6.

From the figure, we can see that at the same voltage, the cation concentration near the membrane of case 1 is minimum, followed by case 2, and finally the case 3. In other words, the ion depletion layer of case 1 is the thickest and this layer is thinner for case 2 and case 3. That explains the I-V curves in Fig. 4, where in case 1 the system enters limiting mode earlier than the rest as analyzed in previous section 4.1 of the paper. In particular, the thicker the ion depletion layer or the

smaller the cation concentration near the membrane, the more hindered ion transport through the membrane. If only considering the desalination capacity of the system, it seems that case 1 is giving the best results but the reality is about the energy efficiency of the desalination. So optimizing the system for the product with satisfactory quality is required. The desalination qualities that are considered in detail in the efficiency coefficients will be discussed in the next sections.
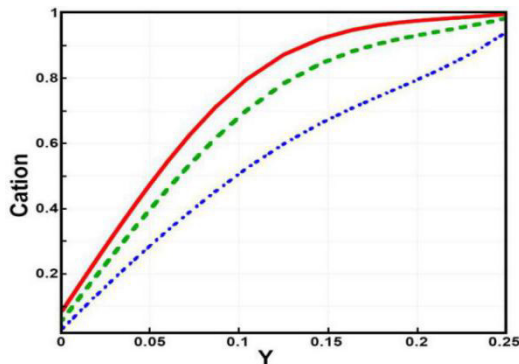


Fig. 6. The distribution of cation concentration according to $Y$ that is perpendicular to the membrane at the dilute channel output at the various feeding-flow velocities. 0.5mm/s (dash-dot line); 1.0mm/s (dash line); 1.5mm/s (solid line).

### 4.3. Effect of Feeding-Flowrate on the Desalination Efficiency

#### 4.3.1. Current efficiency:

We examined the current efficiency of the ED system in the Ohmic, limiting regimes to compare with the experimental result in our previous studies [3]. As shown in [3], in the Ohmic regime, the large variation of the effective current during the voltage increase, where the slope coefficient in ohmic mode is greatest, due to higher currents and constant cell resistance. Whereas, from our current simulation results, thanks to the characteristics of the return flow, the efficient current of the RF-ICP system has positive stability throughout the applied voltage range.

By applying different values of feeding-flow velocity we investigated the effect of this feeding-flow on the system's current efficiency. It shows that input flow is a key parameter for optimizing the desalination system. In all three cases of feeding-flow, the effective current (CE) is greater than 1, at the velocity of 0.5 mm/s of the inlet flow the effective current is ~1.185, these values are ~1.207 and ~1.208 correspond to the input velocity of 1.0 mm/s and 1.5 mm/s. In comparison with the CE of the ED system, which does not exceed 1, it is obvious that the RF-ICP takes advantage of the ED system. As shown in Fig. 7, the increase in the velocity of the feeding-flow leads to an increase in the current efficiency. That is due to the more ions coming into the channel at high feeding-

flow that decrease the system electrical resistance. The simulation result also displays that when the feeding-flow velocity increases from 0.5 mm/s to 1.0 mm/s the CE increases significantly, whereas there is negligible change in CE as the feeding-flow velocity increases from 1.0 mm/s to 1.5 mm/s. This demonstrates that the system reaches a limit of CE as feed flow increases. The limitation in CE relates closely to the limiting current passing through membranes. Whereas the CE of ED does not depend on the inlet flow velocity, the efficient current of the RF-ICP can be controlled via changing feeding-flow thanks to the characteristics of the return flow. Therfore, to optimize this system we need to change the more complex conditions.

As can be seen in Fig. 7, at the velocity of 0.5 mm/s, the current efficiency is almost stable over the voltage range $1\,V_0$ to $37\,V_0$. At the applied voltage value of $38\,V_0$, the current efficiency has a significant decrease and since that value, the current efficiency is unstable as the system starts to enter over the overlimiting regime. Whereas at the values of the feeding-flow rates 1.0 mm/s and 1.5 mm/s the current efficiencies achieve longer stability, that is due to the suppressing depletion effect of the feeding-flow: more ions are carried into the system. When the inlet flow velocity increases from 0.5 mm/s to 1.0mm/s the current efficiency increases significantly, whereas this difference almost disappears as the inlet velocity increases from 1.0 mm/s to 1.5 mm/s. This demonstrates that we have reached the limit of optimization of the RF-ICP system given the velocity of the inlet flow.
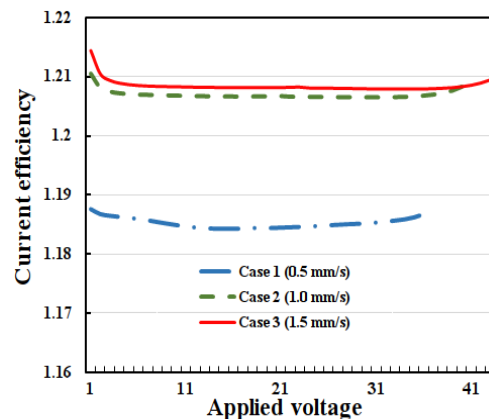


Fig. 7. The current efficiency according to applied voltage at the various feeding-flow velocities: 0.5 mm/s (dash-dot line); 1.0 mm/s (dash line); 1.5 mm/s (solid line).

#### 4.3.2. Salt removal ratio:

The salt removal ratio is a parameter to indicate the desalting ability of devices. This parameter helps to evaluate the correlation between the number of ions removed and the number of ions entered. As the inflow velocity increases, the number of ions removed through the membrane also increases. This has been

demonstrated via the current values at a given applied voltage of the three feeding-flow cases (Fig. 4). In detail, the higher the inlet flow velocity, the higher the value of current on the same voltage value, i.e., the more salt ions carry current through the membrane. However, due to the high inlet flow velocity, the larger the difference between the velocity in the middle part of the flow and the marginal part, the larger the concentration of the outflow resulting in a smaller salt remove ratio.
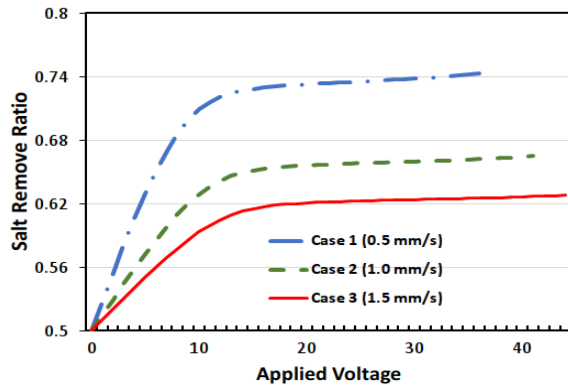


Fig. 8. The change in the salt remove ratio at various flow velocities (0.5, 1.0, 1.5 mm/s).

As can be seen in Fig. 8, the dash-dot line is the graph of the salt remove ratio at the velocity of the inlet flow of 0.5 mm/s, the dash line is the graph at the velocity of 1.0 mm/s, and the solid line is the graph at the velocity of 1.5 mm/s, at low applied voltage, the salt remove ratio increases linearly with the applied voltage. To explain the increase in the salt removal ratio, we start from the definition formula of salt removal ratio, the ion density near the membrane is still high, the number of ions entering the system (the denominator) remains the same, the number of ions removed through the membrane increases (the numerator). In the second regime, when the ionic density of the area near the membrane decreases, even with an increase in the applied voltage, the number of ions detached through the membrane (the numerator) is negligible.

When the feeding-flow velocity increases from 0.5 mm/s to 1.0 mm/s the salt removal ratio decreases 10% (from ~0.73 to ~0.65). However, this value is only approximately 3% when the feeding-flow rate increases from 1.0 mm/s to 1.5 mm/s. So that, the salt removal ratio changes inversely with the feeding-flow rate.

*4.3.3. Energy per ion removal ratio:*

As a result of more ions are brought into the channel with higher feeding velocity, the system required less energy to extract ions. As shown in Fig. 9, when increasing the feeding-flow velocity from 0.5 mm/s to 1.0 mm/s, at the applied voltage of 38 $V_0$, the energy per ion removal decreases ~1.51 (from

~64.46 to ~52.95). When we increase the inlet flow rate from 1.0 mm/s to 1.5 mm/s the difference between the energy required to remove an ion through the membrane is negligible over the applicable voltage range. The difference between the values of the energy per ion removal is only about 1%. Thus, it can be said that this is the smallest limit that the energy per ion removal can be reached.
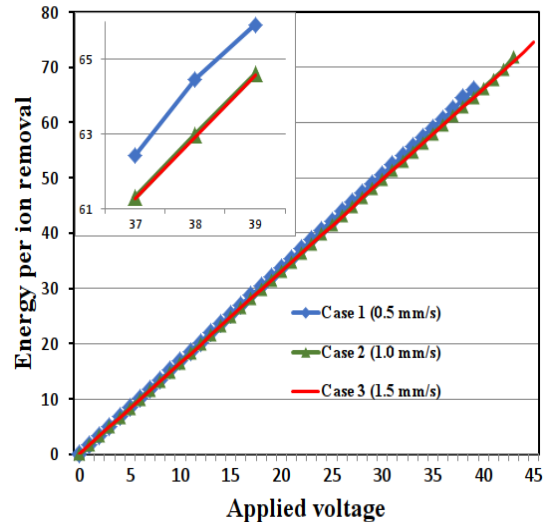


Fig. 9. The energy per ion removal (EPIR) corresponds to the range of the applied voltage at the various feeding-flow velocities. 0.5 mm/s (dash-dot line); 1.0 mm/s (dash line); 1.5 mm/s (solid line).

**5. Conclusion**

In this study, we created a numerical model to investigate the return-flow desalination system's operational procedure in detail. The energy per ion removed decreases as the feeding-flow rate is raised, the salt removal ratio changes inversely with feeding-flow rate, and the simulation results for various feeding-flow rates at various applied voltages show that the current efficiency of the system is better with higher feeding-flow rates. One can use the research's findings to improve the RF-ICP system itself. Inlet/outlet area ratio, channel length, development of overlimiting current regimes, and other factors also affect how well RF-ICP performs. These elements will be investigated in our upcoming study.

**Acknowledgments**

**References**

[1] Panagopoulos, Argyris, K.-J. Haralambous, M. Loizidou, Desalination brine disposal methods and treatment technologies - A review, Science of the Total Environment 693 (2019): 133545.
https://doi.org/10.1016/j.scitotenv.2019.07.351.

[2] Elimelech, M., Phillip, W. A., The future of seawater desalination: energy, technology, and the environment. Science, 333(6043), 712-717, 2011 https://doi.org/10.1126/science.1200488.

[3] Lienhard, J. H., Mistry, K. H., Sharqawy, M. H., Thiel, G. P., Thermodynamics, exergy, and energy efficiency in desalination systems. Desalination Sustainability 127-206. (2017) https://doi.org/10.1016/b978-0-12-809791-5.00004-3.

[4] Kim, B., Choi, S., Pham, V. S., Kwak, R., Han, J.. Energy efficiency enhancement of electromembrane desalination systems by local flow redistribution optimized for the asymmetry of cation/anion diffusivity, Journal of Membrane Science, 524, 280-287. (2017) https://doi.org/10.1016/j.memsci.2016.11.046.

[5] Lattemann, S., Höpner, T., Environmental impact and impact assessment of seawater desalination. Desalination, 220(1-3), 1-15. (2008) https://doi.org/10.1016/j.desal.2007.03.009.

[6] Gregory, K. B., Vidic, R. D., Dzombak, D. A., Water management challenges associated with the production of shale gas by hydraulic fracturing. Elements, 7(3), 181-186. (2011) https://doi.org/10.2113/gselements.7.3.181.

[7] Shaffer, D. L., Arias Chavez, L. H., Ben-Sasson, M., Romero-Vargas Castrillón, S., Yip, N. Y., Elimelech, M., Desalination and reuse of high-salinity shale gas produced water: drivers, technologies, and future directions, Environmental Science & Technology, 47(17), 9569-9583. (2013). https://doi.org/10.1021/es401966e.

[8] Thiel, G. P., Tow, E. W., Banchik, L. D., Chung, H. W., & Lienhard, J. H., Energy consumption in desalinating produced water from shale oil and gas extraction. Desalination, 366, 94-112. (2015). https://doi.org/10.1016/j.desal.2014.12.038.

[9] Vidic, R. D., Brantley, S. L., Vandenbossche, J. M., Yoxtheimer, D., Abad, J. D., Impact of shale gas development on regional water quality, Science, 340(6134), 1235009-1235009. (2013). https://doi.org/10.1126/science.1235009.

[10] Rassenfoss, S., From flowback to fracturing: water recycling grows in the marcellus shale, Journal of Petroleum Technology, 63(07), 48-51. (2011). https://doi.org/10.2118/0711-0048-jpt.

[11] Gregory, K. B., Vidic, R. D., Dzombak, D. A., Water management challenges associated with the production of shale gas by hydraulic fracturing, Elements, 7(3), 181-186. (2011). https://doi.org/10.2113/gselements.7.3.181.

[12] Greenlee, L. F., Lawler, D. F., Freeman, B. D., Marrot, B., Moulin, P., Reverse osmosis desalination: Water sources, technology, and today's challenges. Water Research, 43(9), 2317-2348. (2009). https://doi.org/10.1016/j.watres.2009.03.010.

[13] Strathmann, H., Electrodialysis, a mature technology with a multitude of new applications, Desalination, 264(3), 268-288. (2010). https://doi.org/10.1016/j.desal.2010.04.069.

[14] Kwak, R., Guan, G., Peng, W. K., Han, J., Microscale electrodialysis: Concentration profiling and vortex visualization, Desalination, 308, 138-146. (2013). https://doi.org/10.1016/j.desal.2012.07.017.

[15] Fritzmann, C., Löwenberg, J., Wintgens, T., Melin, T., State-of-the-art of reverse osmosis desalination. Desalination, 216(1-3), 1-76. (2007). https://doi.org/10.1016/j.desal.2006.12.009.

[16] Theodori, G. L., Luloff, A. E., Willits, F. K., Burnett, D. B., Hydraulic fracturing and the management, disposal, and reuse of frac flowback waters: Views from the public in the Marcellus Shale. Energy Research & Social Science, 2, 66-74. (2014). https://doi.org/10.1016/j.erss.2014.04.007.

[17] Yoon, J., Do, V. Q., Pham, V.-S., Han, J., Return flow ion concentration polarization desalination: A new way to enhance electromembrane desalination, Water Research. (2019). https://doi.org/10.1016/j.watres.2019.05.042.

[18] Kwak, R., Pham, V. S., Kim, B., Chen, L., Han, J., Enhanced Salt Removal by Unipolar Ion Conduction in Ion Concentration Polarization Desalination. Scientific Reports, 6(1). (2016). https://doi.org/10.1038/srep25349

[19] Pham, S. V., Kwon, H., Kim, B., White, J. K., Lim, G., Han, J., Helical vortex formation in three-dimensional electrochemical systems with ion-selective membranes. Physical Review E, 93(3). (2016). https://doi.org/10.1103/physreve.93.033114.

[20] Do, Q.-V., Van, D.-A., Nguyen, V.-B., Pham, V.-S., A numerical modeling study on inertial focusing of microparticle in spiral microchannel. AIP Advances, 10(7), 075017. (2020). https://doi.org/10.1063/5.0006975.

[21] Pham, V. S., Li, Z., Lim, K. M., White, J. K., Han, J., Direct numerical simulation of electroconvective instability and hysteretic current-voltage response of a permselective membrane, Physical Review E, 86(4). (2012). https://doi.org/10.1103/physreve.86.046310.

[22] C. Geuzaine and J.-F. Remacle. Gmsh: a three-dimensional finite element mesh generator with built-in pre- and post-processing facilities. International Journal for Numerical Methods in Engineering 79(11), pp. 1309-1331, 2009.